ChemComm

COMMUNICATION

View Article Online
View Journal

Cite this: DOI: 10.1039/d5cc02136g

Received 16th April 2025,
Accepted 15th July 2025

DOI: 10.1039/d5cc02136g

rsc.li/chemcomm

Colorimetric ALP detection with a ligand-exchanged Au_8 cluster†

Jingjing Yang,‡[a] Qing You,‡[b] Qian Wang,‡[a] Hongliang Zhao,[a] Yu Cheng,[a] Ming Yao,[a] Junchi Ruan,[a] Yan Zhao,*[a] Man-Bo Li *[a] and Zhikun Wu *[ab]

An atomically precise Au_8 nanocluster (dppm/dppp) synthesized *via* ligand exchange exhibits oxidase-like activity. Alkaline phosphatase (ALP) quenches $O_2^{\bullet-}$, enabling sensitive and specific colorimetric detection and demonstrating diagnostic potential.

Alkaline phosphatase (ALP) serves as a crucial clinical diagnostic indicator, with abnormal levels associated with hepatic disorders (obstructive jaundice, cholestatic hepatitis), bone diseases (osteoporosis), and cancers.[1] The development of ALP detection methods[2] is important. Current methods are generally based on electrochemistry, chromatography, and fluorescence, which are limited by the need for bulky precision instruments, extended detection times, and complex operational steps. This creates a pressing need for simple, rapid, and sensitive detection strategies. Colorimetry based on nanozymes has emerged as a promising alternative.[3] Nanozymes,[4] nanomaterials with intrinsic enzyme-like catalytic activities, catalyze the conversion of O_2 to reactive oxygen species (ROS), which subsequently oxidize 3,3′,5,5′-tetramethylbenzidine (TMB) to produce blue coloration. Based on the mechanism, a cascade can be established as follows: ALP hydrolyzes 2-phospho-L-ascorbic acid (AAP) to generate ascorbic acid (AA) that acts as a ROS scavenger and effectively suppresses TMB oxidation,[5] enabling quantitative ALP activity measurement through colorimetric signal modulation.

Metal nanocluster-based nanozymes (nanoclusterzymes) have recently garnered significant attention in the field of nanotechnology due to their atomic precision and sensitivity.[6–13] They exhibit remarkable accuracy and efficiency across a broad spectrum of analytical applications, underscoring their potential as valuable tools in catalysis and detection methodologies.[14] The synthesis of atomically precise metal nanoclusters has been a major research focus, with significant advancements in controlling their size, composition, and surface chemistry.[15] Furthermore, integrating nanoclusterzymes into various platforms has expanded their applications.[7,8,12] For example, single-atom regulation of $Au_{25}(SR)_{18}$ resulted in its high antioxidant activity that is approximately 160 and 9 times higher than that of natural vitamin E and antioxidant anthocyanin molecules.[6] The exceptional catalytic performance of nanoclusterzymes allows efficient target reaction catalysis within detection systems, thus enhancing sensitivity and speed. However, current applications of nanoclusterzymes primarily focus on disease treatment, with few reports on their use in biosensing detection fields.[11,16] These studies indicate the vast potential of nanoclusters in detection and sensing systems.

A previous report demonstrates that a diphosphine-protected gold nanocluster $[Au_{14}(Dppp)_5I_4]^{2+}$ efficiently activates O_2 and exhibits oxidase (OXD)-like properties,[11] while it suffers from a stability issue (Fig. S1A, ESI†). Introduction of relatively strong-coordinating thiol ligands would enhance the stability of nanoclusters, but this may compromise their catalytic activity.[17] To strike a balance between nanoclusters' catalytic activity and stability, we selected bis(diphenylphosphino)methane (dppm), a ligand with higher structural rigidity, as the preferred choice for ligand exchange in this study. Fortunately, a more stable nanocluster was synthesized through ligand exchange. Electrospray ionization mass spectrometry (ESI-MS) and single-crystal X-ray diffraction (SCXRD) confirmed the precise composition and structure of this newly formed nanocluster, which exhibits oxidase-like activity under light excitation. By utilizing the ALP enzyme's catalytic reaction, we established a biosensor that provides a novel method for detecting ALP by preventing the oxidation of TMB.

The ligand-exchange synthesis is based on the parent nanocluster $[Au_{14}(Dppp)_5I_4]^{2+}$ (Scheme 1, more details in the ESI†). The reaction mixture was sampled at different time intervals for UV-vis-NIR, ESI-MS and TLC (thin-layer

[a] *Institutes of Physical Science and Information Technology, Key Laboratory of Structure and Functional Regulation of Hybrid Materials of Ministry of Education, Anhui University, Hefei, 230601, China. E-mail: 20231@ahu.edu.cn, mbli@ahu.edu.cn*

[b] *Key Laboratory of Materials Physics, Anhui Key Laboratory of Nanomaterials and Nanotechnology, CAS Center for Excellence in Nanoscience, Institute of Solid State Physics, Hefei Institutes of Physical Science (HFIPS), Chinese Academy of Sciences, Hefei, Anhui 230601, China. E-mail: zkwu@issp.ac.cn*

† Electronic supplementary information (ESI) available. See DOI: https://doi.org/10.1039/d5cc02136g

‡ These authors contributed equally to this work.

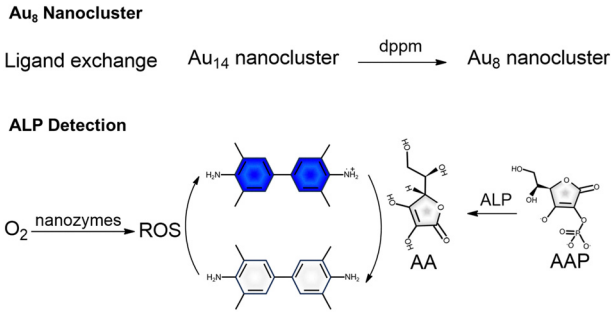

Scheme 1 Schematic of Au_8 synthesis and the ALP detection mechanism.

chromatography) analyses (Fig. S2, ESI†). As shown in Fig. S2A (ESI†), upon addition of dppm, the characteristic absorption peaks at 343 and 436 nm of $Au_{14}(dppp)_5I_4$ disappeared within 5 minutes. After completion of the reaction, four new absorption peaks emerged. Remarkable changes were also observed in ESI-MS and TLC analyses (Fig. S2B and C, ESI†). The UV-vis-NIR spectrum of the purified nanocluster exhibits four notable absorption bands centered at 332 nm (3.73 eV), 410 nm (3.02 eV), 460 nm (2.70 eV) and 522 nm (2.38 eV) (Fig. S3A, ESI†). By extrapolating the lowest energy absorption peak to zero absorbance, the optical energy gap is determined to be ~2.07 eV (inset of Fig. S3A, ESI†). ESI-MS was applied to determine the exact formula of the as-prepared nanoclusters. As shown in Fig. S3B (ESI†), under the positive mode, an exclusive peak at *m/z* 3393.93 was observed, which is assigned to $[Au_8(dppm)_3(dppp)I_2]^+$ (calculated *m/z* 3394.07; deviation, 0.14). This assignment is supported by comparison of the calculated and experimental isotopic patterns (inset of Fig. S3B, ESI†). The purity of the nanocluster was further confirmed by TLC (Fig. S3C, ESI†), X-ray photoelectron spectroscopy (XPS, Fig. S4, ESI†), inductively coupled plasma (ICP, Table S1, ESI†), and thermogravimetric (TGA, Fig. S5, ESI†) analyses.

SCXRD analysis[22] reveals that $[Au_8(dppm)_3(dppp)I_2]^+$ crystallizes in the monoclinic $P\ 2_1$ chiral space group, with two nanoclusters in a unit cell (Fig. S6, ESI†). The chirality originates from the asymmetric arrangement of the ligands on the surface and the metal atoms in the kernel.[18] $[Au_8(dppm)_3(dppp)I_2]^+$ consists of an Au_7 kernel comprising two I atoms, two dppm ligands, and a special staple unit "dppm-Au-dppp", as shown in Fig. 1A. The Au_7 kernel (Fig. 1B) can be visualized as a triangular pyramid Au_4 unit with Au–Au bond lengths ranging from 2.68 to 2.86 Å (Fig. 1C and Fig. S7A, ESI†) fused with a pyramidal Au_5 unit (Au–Au bond lengths range from 2.62 to 2.89 Å, Fig. 1D and Fig. S7B, ESI†) by sharing two gold atoms. Two I atoms (Fig. 1E) are located at both ends of the Au_7 kernel with an average Au–I bond length of 2.91 Å. One dppm ligand binds to the Au_5 unit, while another dppm ligand bridges both the Au_5 and the Au_4 units, reinforcing the connection between them. The distinctive staple of "dppm-Au-dppp"(Fig. 1G) also spans both Au_5 and Au_4 units.

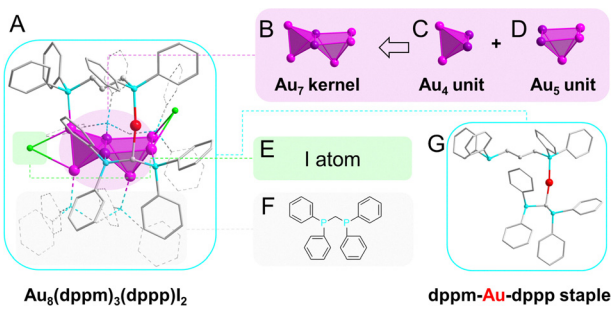

Fig. 1 Analysis of the $[Au_8(dppm)_3(dppp)I_2]^+$ nanocluster structure: (A) the complete structure of $[Au_8(dppm)_3(dppp)I_2]^+$; (B) the Au_7 kernel; (C) the Au_4 unit; (D) the Au_5 unit; (E) I atom; (F) dppm ligand; and (G) the "dppm-Au-dppp" staple. For clarity, H is omitted. Red, magenta and dark purple denote Au, cyan denotes P, gray denotes C, and green denotes I.

Inspired by the previous work where gold atoms in staple motifs are beneficial for catalysis,[11,19] we investigated the enzyme-like activity of the Au_8 nanocluster bearing the special staple unit "dppm-Au-dppp". As shown in Fig. 2A, Au_8 efficiently catalyzed the oxidation of TMB under light irradiation, giving the oxidized product oxTMB with a characteristic absorption peak at 652 nm. Control experiments show that light irradiation is essential, which is also confirmed by the light on-and-off experiments (Fig. 2B). The optimized conditions were found to be pH 4.0, 10 min, TMB and Au_8 concentrations of 1 mM and 150 mg L^{-1}, respectively (Fig. S8, ESI†). Given the swift detection and the fact that the reaction had already achieved 92% completion within the first five minutes, a five-minute time point was consequently chosen for subsequent analyses. Au_8 remained stable at pH 4.0 for 48 h, as shown in Fig. S9 (ESI†). Approximately 65% of its initial OXD-like activity was retained after 6 cycles (Fig. S10, ESI†). The steady-state kinetic assay was performed to obtain the Michaelis–Menten curve and the Lineweaver–Burk plot under the optimal conditions. As shown in Fig. 2C and D, the K_m and V_{max} values were determined to be 0.558 mM and 32.35×10^{-8} M s^{-1}, respectively.

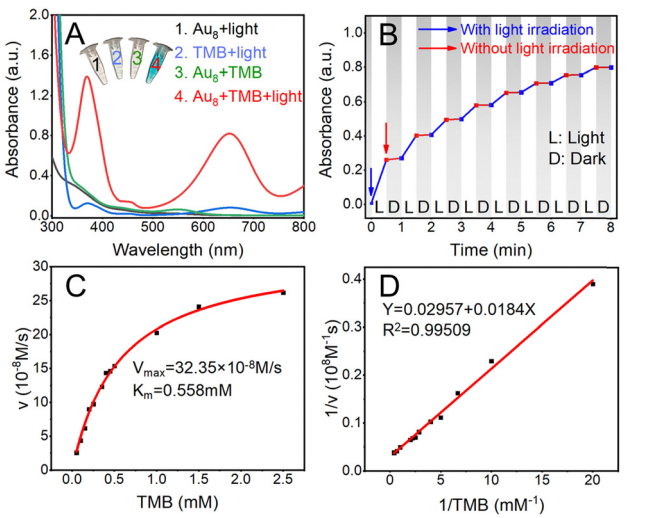

Fig. 2 Catalytic properties of Au_8 (the concentration of Au_8 in the solution is 30 mg L^{-1}): (A) UV-vis absorption spectra of four samples in 0.01 M acetate buffer solution (pH 4.0) containing: (1) Au_8 + light; (2) TMB + light; (3) Au_8 + TMB; and (4) Au_8 + TMB + light. (B) Photo-controllable oxidase-mimicking activity of Au_8. (C) Reaction velocity curves under different TMB concentrations and (D) the corresponding double reciprocal plot.

The above experimental results suggest that Au_8 nanoclusters exhibit OXD-like activity under light irradiation by catalyzing the conversion of dissolved oxygen to generate $O_2^{\bullet-}$ radicals, which act as the real oxidative species for oxidizing TMB. To verify this assumption, we performed the following experiments. First, we conducted the catalytic reaction under atmospheres of nitrogen, oxygen, and air, respectively. As shown in Fig. S11 (ESI†), the chromogenic intensity of Au_8/TMB under N_2, air, or O_2 atmospheres demonstrates that oxygen serves as an essential oxidant in the reaction. Second, various scavengers, including *p*-benzoquinone (PBQ), thiourea and tryptophan (Try), were added to the reaction mixture to confirm the type of reactive oxygen species (ROS) during the oxidase-like reaction. The results showed that only PBQ ($O_2^{\bullet-}$ scavenger) significantly inhibited the catalytic process, suggesting that $O_2^{\bullet-}$ plays an essential role in the catalytic process. The signal for DMPO-$O_2^{\bullet-}$,[11] is clearly observed (Fig. S11C, ESI†) in the Au_8/DMPO system based on the electron paramagnetic resonance (EPR) spectrum, further confirming the generation of $O_2^{\bullet-}$ during the catalytic process. Zeta potential analysis[20] elucidated interactions among Au_8, O_2, and TMB (Fig. S12, ESI†). Upon TMB addition, the potential increased to +23.49 mV, confirming TMB adsorption onto Au_8. Subsequent illumination decreased the potential to +19.58 mV, indicating the $O_2^{\bullet-}$ mediated TMB oxidation and desorption.

To identify the catalytic sites responsible for the OXD-like activity of the Au_8 nanocluster, we conducted Density Functional Theory (DFT) calculations. Three distinct locations were selected for detailed analysis: (a) Au sites within the Au_7 kernel; (b) Au sites on the surface of the Au_7 kernel; and (c) "dppm-Au-dppp" staple ligand site (inset, Fig. 3A). According to the previous DFT studies,[21] five steps are involved in the activation process of O_2 over the catalyst surface. Each process was calculated herein. The initial adsorption of O_2 at the surface Au sites results in the formation of an intermediate species, **int-1** (step i). In step ii, **int-1** is converted to **int-2** through the reduction of O_2* to OOH* (*i.e.*, $O_2^{\bullet-}$), with an associated energy change of −0.48 eV. Following this, the OOH* species undergo further reduction to O* by reacting with a molecule of TMB-H^+, which entails an energy change of −1.50 eV (step iii). Subsequently, the adsorbed O* species can be further reduced to H_2O through steps iv and v, as depicted in Fig. 3. Analyzing the Gibbs free energy in Fig. 3A, each reaction step at the three activation sites is found to exhibit a negative energy change. Notably, activation site (b) (*i.e.*, Au sites on the surface of the Au_7 kernel) demonstrates a more pronounced overall energy reduction compared to the other sites. The marked thermodynamic superiority suggests that oxygen molecules preferentially adsorb on the activation site (b) during catalytic processes. Furthermore, we calculated the adsorption capabilities of TMB at the three sites (a, b, and c) on the nanocluster. As shown in Fig. S14A and B (ESI†), since TMB molecules cannot access site (a), we only performed calculations for sites (b) (−0.22 eV) and (c) (−0.27 eV) (Fig. S14C and D, ESI†). The results indicate that TMB has better adsorption capability at site (c). Collectively, these findings support a synergistic catalytic mechanism: both the Au_7 kernel and the "dppm-Au-dppp" staple in the Au_8 nanocluster significantly contribute to the catalysis by working on oxygen and TMB, respectively.

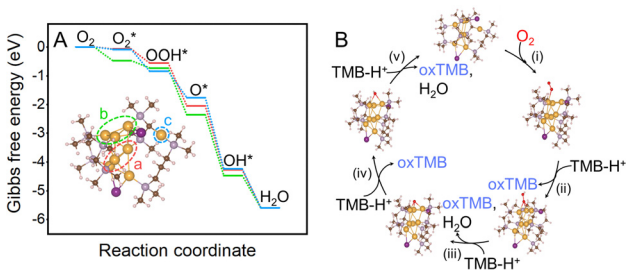

Fig. 3 (A) Corresponding free energy diagram for the OXD-like reaction on three sites. (B) Proposed reaction pathways of O_2 reduction to H_2O with optimized adsorption configurations on the b site of Au_8.

Considering that the reductive properties of AA would inhibit TMB oxidation, we performed quenching experiments to confirm this hypothesis and evaluate the effect of AA during catalysis (Fig. S15, ESI†). Introduction of AA into the Au_8/TMB system led to an immediate decrease in the absorbance of 652 nm (A_{652}) (black and red curves), implying effective suppression of oxTMB formation. Furthermore, when AA was added during the reaction initiation phase (blue curve), a delayed oxidation profile of TMB emerged, persisting until the complete consumption of AA. Strikingly, the slopes of these three curves indicate that the introduction of AA does not significantly impact the catalytic efficacy of Au_8. To achieve highly sensitive AA detection, the concentrations of Au_8 and TMB were optimized. As demonstrated in Fig. S16 (ESI†), 10 mg L^{-1} Au_8 and 0.8 mM TMB were selected as the optimal concentrations for all subsequent experiments. Under the optimized conditions, A_{652} was decreased gradually with the increased concentration of AA added to the (Au_8 + TMB) system (Fig. S17, ESI†), confirming the system's responsiveness to varying levels of AA.

This colorimetric assay for ALP detection is based on an enzyme-like conversion of AAP by ALP into AA, which subsequently reduces oxidized TMB (blue) to colorless oxTMB. Consistent with the mechanism, the blue color disappeared when both ALP and AAP were introduced into the (Au_8 + TMB) system (Fig. 4A). As shown in Fig. 4B and Fig. S18 (ESI†), the decreased amplitude demonstrated a good linear relationship (R^2 = 0.992) with the concentration of ALP in the range from 0 to 10 U L^{-1}, which is comparable to some results reported in the literature (Table S3, ESI†). Selectivity is another important parameter for evaluating the performance of ALP detection. To assess the efficacy of our method for detecting ALP, control experiments were conducted with non-target proteins/enzymes and potential interfering substances. The results, illustrated in Fig. S19 (ESI†), demonstrate that the sensor exhibits selectivity exclusively toward ALP. This high degree of selectivity can be attributed to the high specificity of the enzymatic reaction, which enhances the applicability of this ALP assay in complex samples.

In summary, we synthesized a new nanoclusterzyme, $[Au_8(dppm)_3(dppp)I_2]^+$, *via* a bidentate phosphine ligand

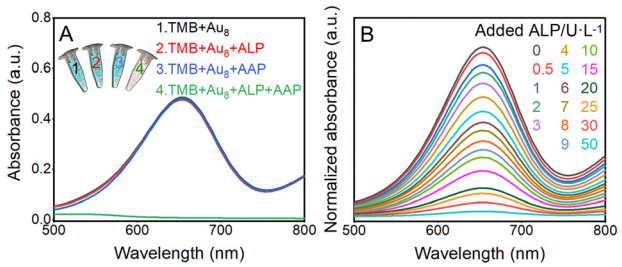

Fig. 4 (A) The feasibility of the Au_8 nanoclusterzyme-based system for ALP detection (AAP (0.05 mM), Au_8 (0.01 mg mL^{-1}), TMB (0.5 mM), and ALP (100 U L^{-1})). (1) TMB + Au_8; (2) TMB + Au_8 + ALP; (3) TMB + Au_8 + AAP; and (4) TMB + Au_8 + ALP + AAP. (B) Relationship between the absorbance of TMB and ALP concentration.

exchange strategy. SCXRD analysis revealed its structure, containing an Au_7 kernel with two I atoms, two dppm ligands, and a unique "dppm-Au-dppp" staple unit. The Au_8 nanocluster exhibits OXD-like activity and efficiently catalyzes the conversion of oxygen to $O_2^{\bullet-}$ under visible light irradiation. The color change of the TMB system was employed to selectively detect ALP at concentrations down to 0.2 mU mL^{-1} (with a signal-to-noise ratio of 3) in a turn-off mode. Additionally, we proposed a detailed oxidase-like catalysis mechanism for the nanocluster, supported by DFT calculations. These findings demonstrate that Au nanoclusterzymes could serve as viable alternatives to natural enzymes for developing highly sensitive colorimetric assays. Overall, our work presents a promising strategy for the rational design of stable nanoclusterzymes with superior oxidase-like activity.

This work was financially supported by the National Natural Science Foundation of China (No. 22471275, 22422101, 22371002, 92061110, 21925303, 21829501, 21771186, and 22405002) and the Key Projects of Anhui Provincial Department of Education (2023AH050056).

Conflicts of interest

There are no conflicts to declare.

Data availability

The data supporting this article have been included as part of the ESI.† We thank the staff members of the Electron Spin Resonance System (**https://cstr.cn/31125.02.SHMFF.ESR**) at the Steady High Magnetic Field Facility, CAS (**https://cstr.cn/31125.02.SHMFF**), for providing technical support and assistance with data collection and analysis.

References

1 (*a*) P. J. O'Brien and D. Herschlag, *Biochemistry*, 2002, **41**, 3207–3225; (*b*) K. Mukaiyama, M. Kamimura, S. Uchiyama, S. Ikegami, Y. Nakamura and H. Kato, *Aging: Clin. Exp. Res.*, 2015, **27**, 413–418; (*c*) C. S. Park, T. H. Ha, M. Kim, N. Raja, H.-S. Yun, M. J. Sung, O. S. Kwon, H. Yoon and C.-S. Lee, *Biosens. Bioelectron.*, 2018, **105**, 151–158.
2 (*a*) T. Hasegawa, M. Sugita, K. Takatani, H. Matsuura, T. Umemura and H. Haraguchi, *Chem. Soc. Jpn.*, 2006, **79**, 1211–1214; (*b*) S. Goggins, C. Naz, B. J. Marsh and C. G. Frost, *Chem. Commun.*, 2015, **51**, 561–564; (*c*) C. Chen, J. Zhao, Y. Lu, J. Sun and X. Yang, *Anal. Chem.*, 2018, **90**, 3505–3511.
3 (*a*) Y. Zhu, J. Wu, L. Han, X. Wang, W. Li, H. Guo and H. Wei, *Anal. Chem.*, 2020, **92**, 7444–7452; (*b*) L. Wu, J. Lin, H. Wang, K. Pan, X. Shi and X. Niu, *Adv. Funct. Mater.*, 2025, **35**, 2413154; (*c*) M. He, X. Xu, H. Wang, Q. Wu, L. Zhang, D. Zhou, Y. Tong, X. Su and H. Liu, *Small*, 2023, **19**, 2208167; (*d*) B. Wang, S. Pu, B. Ma, X. Zou, Q. Xiong, X. Hou and K. Xu, *Anal. Chem.*, 2024, **96**, 18718–18726.
4 (*a*) L. Gao, J. Zhuang, L. Nie, J. Zhang, Y. Zhang, N. Gu, T. Wang, J. Feng, D. Yang, S. Perrett and X. Yan, *Nat. Nanotechnol.*, 2007, **2**, 577–583; (*b*) H. Wei and E. Wang, *Anal. Chem.*, 2008, **80**, 2250–2254; (*c*) M. Li, J. Chen, W. Wu, Y. Fang and S. Dong, *J. Am. Chem. Soc.*, 2020, **142**, 15569–15574; (*d*) Y. Huang, J. Ren and X. Qu, *Chem. Rev.*, 2019, **119**, 4357–4412.
5 X. Sang, S. Xia, L. Cheng, F. Wu, Y. Tian, C. Guo, G. Xu, Y. Yuan and W. Niu, *Small*, 2024, **20**, 2305369.
6 H. Liu, Y. Li, S. Sun, Q. Xin, S. Liu, X. Mu, X. Yuan, K. Chen, H. Wang, K. Varga, W. Mi, J. Yang and X.-D. Zhang, *Nat. Commun.*, 2021, **12**, 114.
7 Y. Hua, J.-H. Huang, Z.-H. Shao, X.-M. Luo, Z.-Y. Wang, J.-Q. Liu, X. Zhao, X. Chen and S.-Q. Zang, *Adv. Mater.*, 2022, **34**, 2203734.
8 H. Ma, X. Zhang, L. Liu, Y. Huang, S. Sun, K. Chen, Q. Xin, P. Liu, Y. Yan, Y. Wang, Y. Li, H. Liu, R. Zhao, K. Tan, X. Chen, X. Yuan, Y. Li, Y. Liu, H. Dai, C. Liu, H. Wang and X.-D. Zhang, *Sci. Adv.*, 2023, **9**, eadh7828.
9 H. Shan, J. Shi, T. Chen, Y. Cao, Q. Yao, H. An, Z. Yang, Z. Wu, Z. Jiang and J. Xie, *ACS Nano*, 2023, **17**, 2368–2377.
10 L. Chen, Y. Du, Y. Lv, D. Fan, J. Wu, L. Wu, M. Cui, H. Yu and M. Zhu, *Nano Res.*, 2023, **16**, 7770–7776.
11 H. Zhao, Q. You, W. Zhu, J. Li, H. Deng, M.-B. Li, Y. Zhao and Z. Wu, *Small*, 2023, **19**, 2207936.
12 Y. Zhao, S. Zhuang, L. Liao, C. Wang, N. Xia, Z. Gan, W. Gu, J. Li, H. Deng and Z. Wu, *J. Am. Chem. Soc.*, 2020, **142**, 973–977.
13 J. Fan, X. Zhang, W. Tan, Z. Feng and K. Li, *Nano Lett.*, 2024, **24**, 7800–7808.
14 (*a*) R. Jin, C. Zeng, M. Zhou and Y. Chen, *Chem. Rev.*, 2016, **116**, 10346–10413; (*b*) P. D. Jadzinsky, G. Calero, C. J. Ackerson, D. A. Bushnell and R. D. Kornberg, *Science*, 2007, **318**, 430–433; (*c*) Y. Lei, F. Mehmood, S. Lee, J. Greeley, B. Lee, S. Seifert, R. E. Winans, J. W. Elam, R. J. Meyer, P. C. Redfern, D. Teschner, R. Schlögl, M. J. Pellin, L. A. Curtiss and S. Vajda, *Science*, 2010, **328**, 224–228; (*d*) Q. Tang, G. Hu, V. Fung and D.-E. Jiang, *Acc. Chem. Res.*, 2018, **51**, 2793–2802; (*e*) Y. Zhu, H. Qian, B. A. Drake and R. Jin, *Angew. Chem., Int. Ed.*, 2010, **49**, 1295–1298.
15 (*a*) Q. Yao, M. Zhu, Z. Yang, X. Song, X. Yuan, Z. Zhang, W. Hu and J. Xie, *Nat. Rev. Mater.*, 2025, **10**, 89–108; (*b*) Y. Cao, T. Liu, T. Chen, B. Zhang, D.-E. Jiang and J. Xie, *Nat. Commun.*, 2021, **12**, 3212; (*c*) L. Feng, Z.-M. Zhu, Y. Yang, Z. He, J. Zou, M.-B. Li, Y. Zhao and Z. Wu, *Acta Phys. Chim. Sin.*, 2024, **40**, 2305029.
16 S. Wang, Z. Li, M. Xia, X. Zhao, C. Chen, Y. Jiang, P. Ni and Y. Lu, *Chem. Res. Chin. Univ.*, 2023, **39**, 907–914.
17 (*a*) W. Fei, Y. Tao, Y. Qiao, S.-Y. Tang and M.-B. Li, *Polyoxometalates*, 2023, **2**, 9140043; (*b*) R. H. Adnan, J. M. L. Madridejos, A. S. Alotabi, G. F. Metha and G. G. Andersson, *Adv. Sci.*, 2022, **9**, 2105692.
18 Y. Guo, Z. Zhang, H. Han and Z. Zhou, *Nano Lett.*, 2024, **24**, 11985–11991.
19 H. Shen, Q. Wu, S. Malola, Y.-Z. Han, Z. Xu, R. Qin, X. Tang, Y.-B. Chen, B. K. Teo, H. Häkkinen and N. Zheng, *J. Am. Chem. Soc.*, 2022, **144**, 10844–10853.
20 H. Li, S. Zhao, Z. Wang and F. Li, *Small*, 2023, **19**, 2206465.
21 (*a*) X. Shen, W. Liu, X. Gao, Z. Lu, X. Wu and X. Gao, *J. Am. Chem. Soc.*, 2015, **137**, 15882–15891; (*b*) Z. Wang, X. Shen and X. Gao, *J. Phys. Chem. C*, 2021, **125**, 23098–23104.
22 Jingjing Yang CCDC 2440091: Experimental Crystal Structure Determination, 2025, DOI: **10.5517/ccdc.csd.cc2mx3m9**.

